Ablation of Carbonaceous Materials in a Hydrogen-Helium Arcjet Flow

Chul Park,* J. H. Lundell,† M. J. Green,* W. Winovich,‡ and M. A. Covington*
NASA Ames Research Center, Moffett Field, California

The stagnation-point ablation rates of a graphite, a carbon-carbon composite, and four carbon-phenolic materials are measured in an arcjet wind tunnel with a 50% hydrogen/50% helium mixture as the test gas. Flow environments are determined through measurements of static and impact pressures, heat-transfer rates to a calorimeter, and radiation spectra, and through numerical calculation of the flow through the wind tunnel, spectra, and heat-transfer rates. The environments so determined are: impact pressure $\cong 3$ atm, Mach number $\cong 2.1$, convective heat-transfer rate $\cong 14$ kW/cm^2, and radiative heat-transfer rate $\cong 7$ kW/cm^2 in the absence of ablation. Ablation rates are determined from the measured rates of mass loss and recession of the ablation specimens. Compared with the predicted ablation rates obtained by running RASLE and CMA codes, the measured rates are higher by about 15% for all tested materials.

Introduction

LATER in this decade, a spacecraft, named Galileo Probe, is expected to enter the atmosphere of the planet Jupiter. Its heat shield is made of two types of carbon-phenolic materials, i.e., chop-molded carbon-phenolic (CMCP) for the spherical nose and tape-wrapped carbon-phenolic (TWCP) for the conical frustum. The thickness of the heat shield is determined so as to accommodate the theoretically predicted entry heating environments.[1] Two groups of computer codes are involved in this prediction, i.e., flow environment codes such as HYVIS, COLTS, and RASLE and the materials-response code CMA.[1,2] The three flow environment codes use nearly the same physical models and predict approximately the same heat-transfer rates to the heat shield surface.[2]

In addition to the numerical calculations, the performance of the heat shield materials is determined experimentally. For the stagnation region where the heating rate is expected to be the highest, three types of experiments have been carried out to verify the validity of the numerical techniques for this region; i.e., laser irradiation,[3,4] ballistic range,[5,6] and arcjet wind-tunnel tests. A gasdynamic laser was used in producing both very-high-intensity tests (up to 1000 kW/cm^2) and moderate-intensity (8-32 kW/cm^2) radiative heat fluxes.[3,4] The fluxes produced by the moderate-intensity tests are comparable to those encountered in the Jovian entry flight. However, since boundary-layer characteristics and spectra of incident radiation in this experiment are different from the Jovian case, the experiment was unable to test the radiative blockage phenomenon in the ablation layer, which is an important parameter.

In the ballistic range experiment, radiative heat-transfer rates slightly higher than the Jovian flight values are produced by using argon as the test gas. This experiment produced incident radiation spectra and the radiative blockage phenomenon in the boundary layer that resembled the Jovian case, but the heating history was much different: the heating was abrupt and the thermal gradient in the test material was much larger than in the Jovian flight.

In the third type of experiment, ablation rates are measured in an arcjet wind tunnel. Unlike the above two methods, this method produces boundary-layer flows and heating rate histories that resemble those in Jovian flight. Moreover, spectra of radiation incident on the wall can be made identical to the Jovian case if the wind tunnel is operated with a hydrogen/helium mixture. The thermal conductivities of hydrogen and helium are both high: hence, when heated, the mixture tends to lose heat rapidly by conduction to the wall. Consequently, in order to produce temperatures sufficiently high to conduct a steady electric current, the electrical power input per unit volume must be greater than a certain critical value. A special wind tunnel, the Giant Planet Facility (GPF), was constructed at Ames Research Center in order to meet this requirement.

The Giant Planet Facility heats a 50% hydrogen/50% helium (by volume) mixture in a constricted arc and expands it through a diverging nozzle to a low supersonic Mach number. Construction, operational characteristics, and flow diagnosis in this facility have been reported by Winovich and Carlson.[7] The flow diagnosis included measurements of static pressures along the expanding nozzle, impact pressure, and total and radiative component only of the heat-transfer rates to a nonablating blunt-body calorimeter made of tungsten. Preliminary results of ablation tests in this facility and the accompanying analysis have been reported by Davy et al.[8] and Green and Davy.[9]

Since then, a series of comprehensive measurements has been made to determine the ablation rates of the two types of carbon-phenolic materials used for Galileo Probe. A graphite and a carbon-carbon composite material have also been tested for comparison. Simultaneously, spectrometric diagnosis was carried out to determine experimentally the thermodynamic state of the test flow. It is the primary purpose of the present work to report the results of these experiments and of the analytical work that accompanies them.

In the work of Green and Davy,[9] the numerical prediction of ablation rates was attempted. A computer code named ARCFLO was developed to solve the problem of flow through the constricted arc. The thermodynamic conditions of the freestream flow in the test section were determined from the pressure of the test section box and the impact pressure, assuming that enthalpy remains unchanged through the expanding nozzle. The analysis led to a Mach number value of 1.2 in the freestream. The flow environment code RASLE and the materials response code CMA were then run

---

Presented as Paper 83-1561 at the AIAA 18th Thermophysics Conference, Montreal, Canada, June 1-3, 1983; received June 20, 1983; revision submitted Dec. 1, 1983.

*Research Scientist. Member AIAA.

†Assistant Chief, Thermo- and Gas-Dynamics Division. Member AIAA.

‡Research Scientist.

for these conditions to predict the ablation rates. The ablation rates so obtained were higher than the measured values.

The validity of the early analysis is questionable because 1) the test section box pressure is not a good indication of the true static pressure in a supersonic jet, and 2) it is not known whether the two pressure values (box and impact) are compatible with the law of momentum conservation in the expanding nozzle. It was felt necessary, therefore, to repeat the calculation with a different approach. In the present work, the process of expansion through the nozzle is calculated by integrating the momentum equation. Radial heat conduction is also accounted for in order to determine the centerline enthalpy more accurately. The expansion calculation is carried out using a code to be identified as ARCNOZ. As will be shown later, the calculation leads to a Mach number of about 2.1 instead of 1.2. The RASLE and CMA calculations are then repeated for the new conditions. In doing so, the new sets of thermodynamic property data for C_2H, C_3H, and C_4H are accommodated.[10] For comparison with the calorimeter data, the RASLE calculation is made for the nonablating case also. For comparison with the spectrometric data, the spectral intensities are calculated theoretically by carrying out a volume integration of radiation emission.

The present work collates all these experimental and theoretical results. It shows that the calculated spectra and the heat-transfer rates to the calorimeter agree closely with the experimental data. The present work compares the experimental ablation rates with the calculated values. Only a small difference was found between the theoretical and experimental ablation rate values. The present results are then compared with those obtained by the laser irradiation and ballistic range experiments. Good agreement is found between the present results and the two previous results. The adequacy of the heat shield for the nose region of Galileo Probe is also discussed.

Experiment

Facility

The geometry of the wind tunnel is shown schematically in Fig. 1a. As shown, the arc constrictor has a diameter of 6 cm and length of 432 cm. The constrictor is followed by a divergent nozzle with a length of 33 cm and area ratio of 1.36. The 50% hydrogen/50% helium (by volume) mixture is injected into the arc heater from the holes uniformly distributed along the constrictor length. In addition, argon is injected into the upstream end of the constrictor at a flow rate equivalent to 0.75% (by volume) of that of the hydrogen/helium mixture. The presence of argon is ignored in the present calculation. A cluster of cathodes is located at the upstream end. Four anodes are located outside the nozzle exit. Nitrogen is injected into the test section box in order to maintain a pressure of about 1 atm there. Further details of the device are described by Winovich and Carlson.[7]

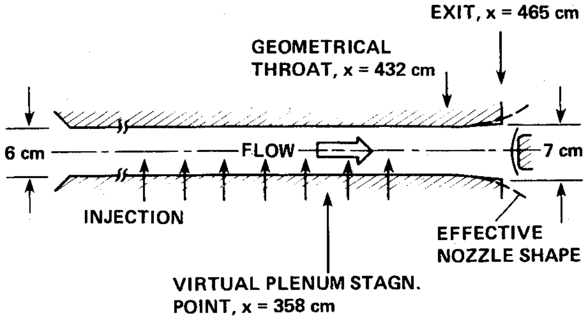

(a) GPF GEOMETRY

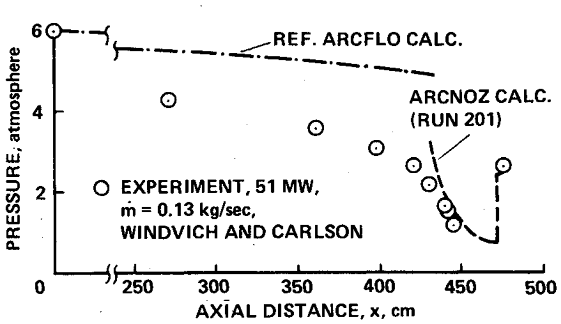

(b) PRESSURE VARIATION

Fig. 1 Geometry of Giant Planet Facility and pressure variation.

Pressures

Static pressure is measured through the pressure ports on the constrictor wall during a run. A typical measured pressure profile is shown in Fig. 1b for an electrical power input of 51 MW and test gas mass flow rate of 0.13 kg/s. As shown, pressure falls rapidly along the axis after $X = 358$ cm. The $X = 358$ cm point is taken to be the virtual plenum stagnation point. The measured impact pressures at the model location varied from 68% of the virtual stagnation value at lower power levels to 62% of the stagnation value at high power levels.

Heat-Transfer Measurement

Heat-transfer rates at the stagnation point are determined from the temperature rise in a thin tungsten wafer forming the surface of a blunt body before it melts and evaporates. The blunt-body calorimeter is in the shape of a slightly curved disk, with a diameter of 4 cm and a surface radius of curvature of 20 cm. The calorimeter normally has a shiny surface and measures the sum of the convective heat-transfer rate and the radiative rate, multiplied by the average absorptivity of the surface. The average absorptivity of the tungsten surface is determined through a separate experiment to be about 0.78. In order to measure the radiative component of heat transfer, the calorimeter is blackened and is covered with a Teflon sheath 1 mm thick. The transmission characteristics of the sheath are measured separately and are corrected for in the determination of the radiative heat flux to the wall. The

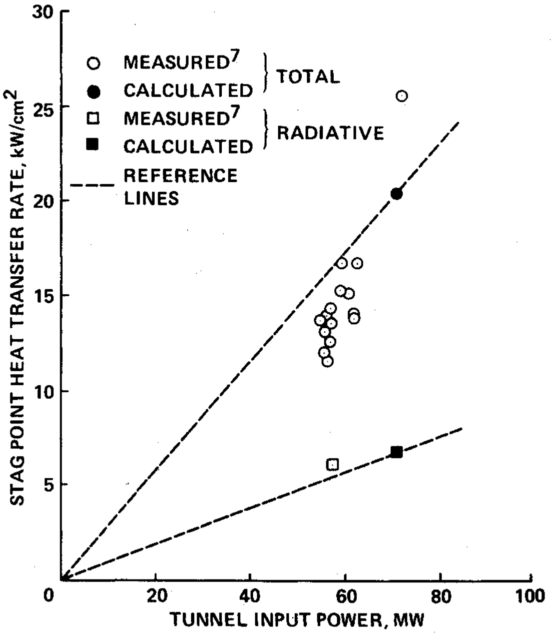

Fig. 2 Comparison between the measured and calculated heat-transfer rates to the nonablating calorimeter (experimental data taken at mass flow rates between 0.12 and 0.17 kg/s; theoretical points are for mass flow rate of 0.16 kg/s).

calorimeter is mounted on one of the four stings equipped in the test section box. East sting is on an arm hinged at a corner of the test section box and stays initially outside the wind-tunnel flow stream. It swings into the center position after the flow is established. Figure 2 shows the results of these heat-transfer measurements.

Except for the one point at 72 MW of input power, all data points for the total heat-transfer rate lie within a small range, which indicates a good reproducibility of the experiment. The radiative component is less than half of the total heat-transfer rate. One can synthesize the true total wall heat-transfer rates by first separating the total heat-transfer rates into convective and radiative components, dividing the radiative components by the surface absorptivity (0.78), and adding them back together. The total heat-transfer rates so determined are approximately 15% higher than the values shown.

Spectrometric Measurement

Spectrometric observation is made of the shock layer from a viewing port located at the position shown schematically in Fig. 3. Radiation emittted from the shock layer over the calorimeter, or the impact pressure probe of identical geometry as the calorimeter, is collected at one end face of a fused-quartz fiber-optic light pipe as shown in the figure. The other end of the light pipe faces the entrance slit of a Tektronix J20 rapid-scanning spectrometer. In this instrument, the dispersing grating is fixed and wavelength scan is achieved by electronically scanning over the voltage outputs from a vidicon image tube placed at the exit focal plane. The electronic signals so obtained are displayed on a storage oscilloscope. At the highest wavelength resolution used in the present work, the wavelength resolution is 0.4 nm. One wavelength scan requires 4 ms at the fastest scan rate.

Figure 4 shows such typical data. The horizontal and vetical axes of the oscillograms correspond to wavelength and spectral intensity, respectively. Different traces indicate different scans made during the same run. Intensities of these traces differ because of the transient phenomenon. The model could have been still in the process of moving into the central position when the first scan was initiated. Or alternatively, the sensitivity of the vidicon is rising from a low initial value to the final high value: due to a peculiarity of vidicon, sensitivity is affected by the history of the average signal level and varies slowly when the signal level changes. In either case, the casue of initially low signal is due to low radiation level of the freestream. The thermodynamic state of the shock layer flow is represented by the trace with the highest intensity.

As seen in Fig. 4a, the Balmer series lines H_γ and H_δ at 433 and 410 nm of hydrogen are the only significant features in the wavelength range of 380-460 nm. Hydrogen lines of shorter wavelengths and the edge of the free-bound continuum at 390 nm expected in this wavelength range are missing due to instrument cutoff. Grating efficiency and transmission of the fiber-optic light pipe degrade rapidly at the short wavelengths for this particular instrument setting. As mentioned in the above section on the facility, argon is present in the test stream. Argon has strong lines in the same wavelength range. Yet no argon line is seen here. This is because 1) molar concentration of argon is small compared with that of hydrogen, and 2) the excited states of argon from which the argon lines emanate are at energy levels considerably higher (by 2 eV) than those of hydrogen lines. In the wavelength range of 465-510 nm shown in Fig. 4b, the H_β line is the only significant spectral feature.

Ablation Measurements

Ablation measurements are made with flat-faced blunt-body models. The overall diameter of the models is 4 cm with the corners rounded to a radius of 0.16 cm. The models consist of two parts: an inner core and an outer shroud. The

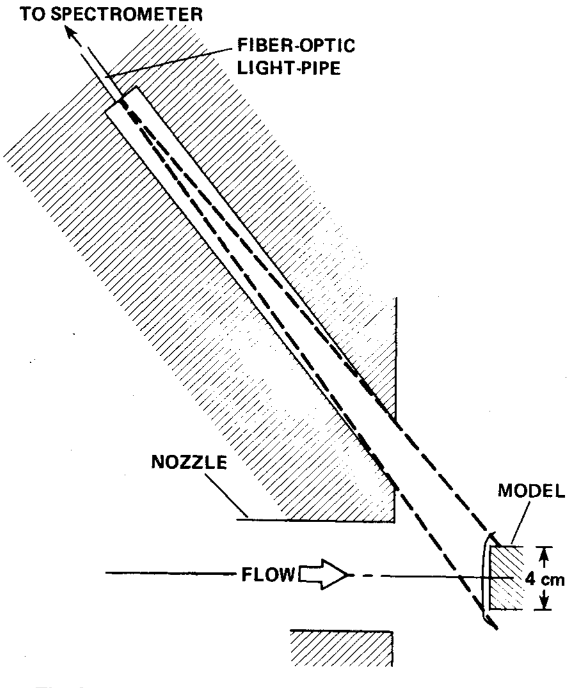

Fig. 3 Optical layout of spectroscopic measurement.

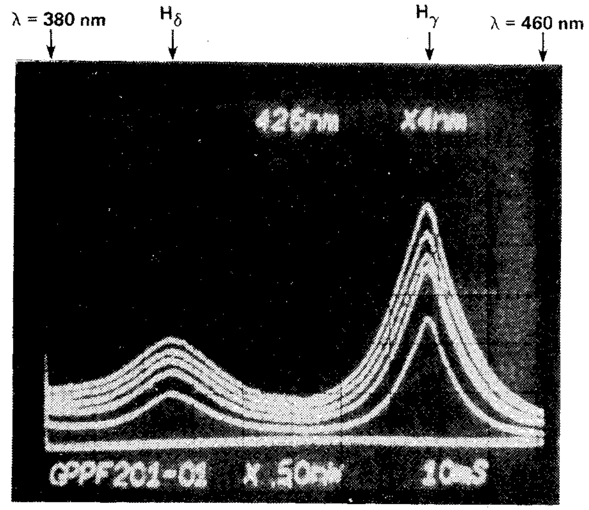

(a) 380 < λ < 460 nm, RUN 201

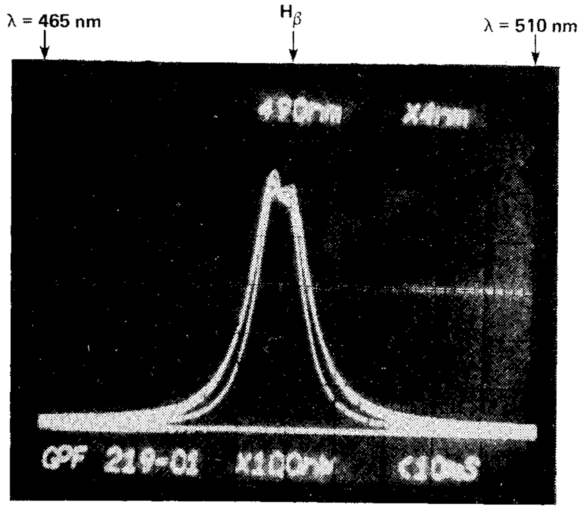

(b) 465 < λ < 510 nm, RUN 219

Fig. 4 Oscillogram record of spectral intensities of shock layer radiation.

inner core is a cylindrical slug 2 cm in diameter, approximately 2 cm long. The core and the shroud are made of the same material and form a smooth flat test surface when assembled. The core is weighed prior to an ablation test. The models are mounted on the stings mentioned earlier. Two or three models are tested in this way during a single run. In some cases, the ablation tests are preceded by impact pressure or calorimeter heat-transfer rate measurements. Such instruments and ablation test models are brought into the stream only after the wind-tunnel flow is fully established. The ablation models are brought out of the test stream after a preprogrammed time interval. The duration of the ablation tests is varied between 1 and 7 s. After the test, the core slug is weighed to determine the change in mass. By dividing the mass change by the wet surface area, mass loss per unit area Δm (in g/cm^2) is obtained. Geometrical recession is also measured to compare with the mass loss data. Recession and mass loss are found to be related consistently through the average density of the material.

The ablation was conducted for 18 ATJS graphite models, 3 multidimensional carbon-carbon composite models, 3 chop-molded carbon-phenolic models with type FM5055A prepreg, 3 chop-molded carbon-phenolic models with type FM5055G prepreg, 3 tape-wrapped carbon-phenolic models with type FM5055A prepreg, and 3 tape-wrapped carbon-phenolic models with type FM5055G prepreg. The chop-molded and tape-wrapped carbon-phenolic with FM5055G prepreg are the same materials as those used on Galileo Probe. In testing the tape-wrapped carbon-phenolic, the planes of the tape cloths were at 30 deg to the ablating surface as they are on the Galileo Probe.

The ablation tests are conducted at a fixed wind-tunnel condition of electrical power input of 71 MW on the average and test gas mass flow rate of 0.160 kg/s. In Figs. 5 and 6, the mass loss Δm obtained from the tests is plotted vas the test duration. As seen in the figures, the mass losses are reproducible and consistent. Recession occurs smoothly with time. The post-test examination revealed a smooth ablated surface for all tested models. Surface roughness was no more than the intrinsic roughness of the fibrous structure of the materials. No sign of massive spallation was seen.

Theory

Calculation of Flow Conditions

As mentioned in the Introduction, the code ARCFLO was used in calculating the flow through the arc constrictor.[9] This code rigorously applies the mass and energy conservation laws, but fails to apply the momentum conservation law. This is because the momentum balance is dictated strongly by turbulence, which is not well understood, and the code is numerically parabolic with respect to axial distance and hence cannot accommodate pressure feedback occurring in a subsonic flow. Because of these limitations, the code cannot accommodate the total wall injection of the test gas. The closest to the real case is obtained under the assumption that 50% of the test gas is introduced in the upstream end and the remainder of the gas from the wall. A best agreement between the calculated and measured arc-heater performance was found with the assumption that the effective turbulent viscosity and thermal conductivity are three times their laminar values. This solution will be referred to as the reference ARCFLO solution.

General features of the reference ARCFLO solution are listed in Table 1. The solution shows that rapid changes in flow properties in the radial direction occur within the outermost 4% of the length of the constrictor radius containing laminar sublayer. The inner 96% of the radius is

Table 1 Measured[a] and calculated flow properties

	Cases			
Property	ARCFLO reference	Run 201	Run 219	Ablation test
Electric power input, MW	60.9	53.6*	67.9*	71.0*
Mass flow rate, kg/s	0.132	0.121*	0.168*	0.160*
Pressure, atm				
Virtual stagnation point	5.49	3.51*	4.82*	4.94*
Throat	5.03	3.22	4.42	4.53
Test section box		1.04*	1.06*	1.05*
Impact		2.39*	3.04*	3.11*
Centerline enthalpy, MJ/kg				
Throat, static	402	3.94	360	400
Throat, kinetic	8.4	11.4	11.7	10.1
Freestream, static		250	225	260
Freestream, kinetic		199	120	125
Behind normal shock, static		363	339	379
Behind normal shock, kinetic		5.8	5.7	6.0
Centerline/average static enthalpy				
Throat	2.12	2.02	2.10	2.16
Freestream		1.51	1.49	1.48
Centerline $\gamma = C_p/C_v$				
Throat	1.099	1.095	1.099	1.099
Freestream		1.098	1.122	1.096
Centerline Mach number				
Throat	0.404	0.580	0.586	0.530
Freestream		2.14	2.17	2.17
Test section ($0 \leq r \leq 1.5$ cm) average				
Density, kg/m^3		8.49^{-4}	1.11^{-3}	1.01^{-3}
Velocity, km/s		15.0	14.9	15.8
Static enthalpy, MJ/kg		219	194	260
Temperature, K		10,630	9,900	10,840
Electron density, cm^{-3}		1.22^{16}	8.32^{15}	1.63^{16}
Shock layer ($0 \leq r \leq 2.0$ cm) average				
Temperature, K		13,590	13,240	13,950
Electron density, cm^{-3}		1.42^{17}	1.47^{17}	1.92^{17}

[a] Measured properties noted with an asterisk.

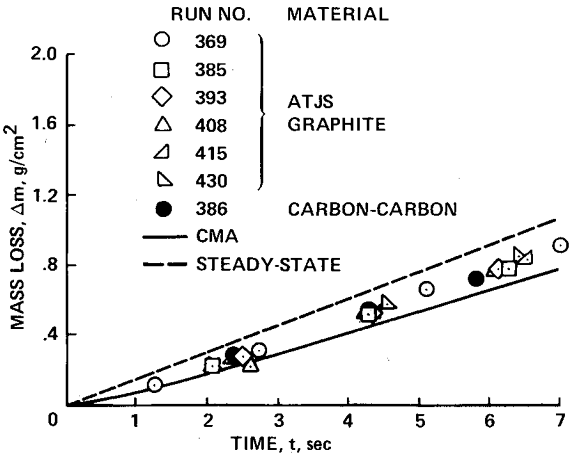

Fig. 5 Comparison between theory and experiment on mass loss rate for ATJS graphite and carbon-carbon composite models.

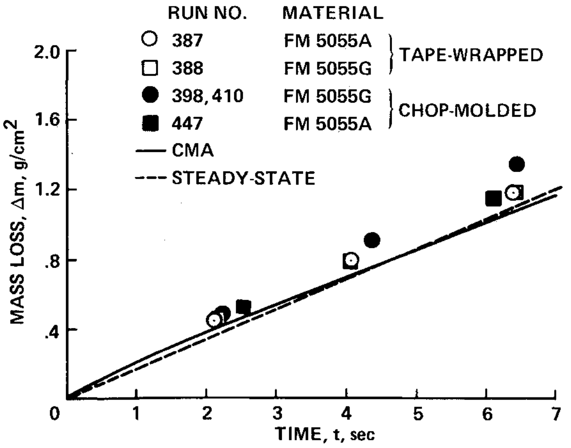

Fig. 6 Comparison between theory and experiment on mass loss rate for carbon-phenolic models.

occupied by a turbulent core flow in which properties change gradually. The pressures obtained by the solution, shown in Fig. 1b, agree with experiment in the first two-thirds of the length of the constrictor. In the downstream third, the calculated pressures are higher than the measured values because of the above-mentioned limitations.

In order to determine the flow conditions at the model location, one needs a code that applies momentum balance in the expanding region correctly and joins with the ARCFLO solution at the throat with an appropriate correction for pressure there. Such a code needs to be accurate only in the centerline region of the flow where the model is located. A code named ARCNOZ is developed for this purpose under the following assumptions:

1) Pressure is constant in the radial direction and is prescribed in the axial direction.

2) Electrical power input and radiative power loss are equal and cancel each other.

3) Wall is adiabatic and frictionless.

4) Nozzle divergence angle is so small that cosine of the angle can be taken as 1.

Assumption 2 is derived from the observation that, both theoretically and experimentally, electrical power input nearly equals the heat loss to the wall in the downstream portion of the constricted-arc flow. Assumption 3 is made because, over the short distance of expansion, the wall heat transfer and wall friction cannot influence the conditions in the centerline region. Under this assumption, the slopes are zero at the wall for both the velocity and enthalpy profiles, which greatly simplifies the analysis.

The equations to be solved are

$$\rho U\frac{\partial U}{\partial x} = -\frac{\mathrm{d}p}{\mathrm{d}x} + \frac{1}{r}\frac{\partial}{\partial r}\left(r\mu\frac{\partial u}{\partial r}\right)$$

$$\rho U\frac{\partial h}{\partial x} = U\frac{\mathrm{d}p}{\mathrm{d}x} + \frac{1}{r}\frac{\partial}{\partial r}\left[rk\frac{\partial T}{\partial r} + \frac{r}{2}\left(\mu - \frac{k}{C_p}\right)\frac{\partial U^2}{\partial r}\right]$$

where ρ, U, p, h, T, and C_p are the density, axial velocity, pressure, static enthalpy, temperature, and specific heat at constant pressure, respectively. The quantities ρ and k are viscosity and thermal conductivity, respectively, which are taken to be three times the laminar values as they are for ARCFLO. The flow is assumed to be in equilibrium. Pressure variation along the axis is assumed to occur as if the test gas were perfect with $\gamma = C_p/C_v = 1.4$ and passed through a hyperbolic nozzle of cross-sectional area A described by $A/A^* = 1 + BX^2$, A^* being the throat area. Figure 1a shows the profile of such a nozzle. Figure 1b shows a pressure profile corresponding to such a nozzle. The Rankine-Hugoniot relationship and the subsonic compression process behind the shock are solved in order to calculate the impact pressure at the centerline. The parameter B in the area ratio specification is varied arbitrarily until the calculated impact pressure agrees with the measured value. The procedure yields flow velocity in the test section. The velocity so determined is weakly dependent on the assumed γ value.

The calculation requires velocity and enthalpy profiles at throat as inputs. The initial profiles for the experimental conditions are derived from the reference ARCFLO solution under the assumption that the velocity and total enthalpy profiles at the throat are similar between the theoretical and experimental cases. Under this assumption, the experimental profiles can be obtained by multiplying the ARCFLO profiles by the following correction factors at each radial point:

$$\frac{\text{Experimental total enthalpy}}{\text{ARCFLO total enthalpy}} = \frac{\text{experimental power input}}{\text{ARCFLO power input}} \times \frac{\text{ARCFLO mass flow rate}}{\text{experimental mass flow rate}}$$

$$\frac{\text{Experimental velocity}}{\text{ARCFLO velocity}} = \frac{\text{ARCFLO pressure}}{\text{experimental pressure}} \times \frac{\text{experimental mass flow rate}}{\text{ARCFLO mass flow rate}}$$

The equations are solved numerically. In Fig. 7, the resulting radial variation of the static enthalpy, temperature, and velocity are shown at the throat and at the test section for the ablation test conditions. In addition, the conditions behind a normal shock wave are shown for the centerline region. As shown in the figure, the virtual wall radius changes from 3 cm at the throat to 4.93 cm at the test section, corresponding to an area ratio of 2.7. This is substantially larger than the geometrical area ratio of 1.36 and is believed to be due to the nonuniform radial distribution of the properties seen in the figure.

The ARCNOZ solution is obtained for runs 201 and 219 referred to in Fig. 4 and for the average conditions of the runs made for the ablation measurement. The results are summarized in Table 1. In the table, the static pressure of the freestream in the test section is lower than the pressure in the test section box. This condition is possible because a portion of the dynamic pressure of the jet flow can be converted to static pressure: only about one-third of the ρU^2 in the jet needs to be converted to static pressure in order for these two pressures to balance. The Mach number at the centerline of the test section is between 2 and 2.2.

As seen in Fig. 7, flow properties vary across the test section. As will be described later, the present ablation rate

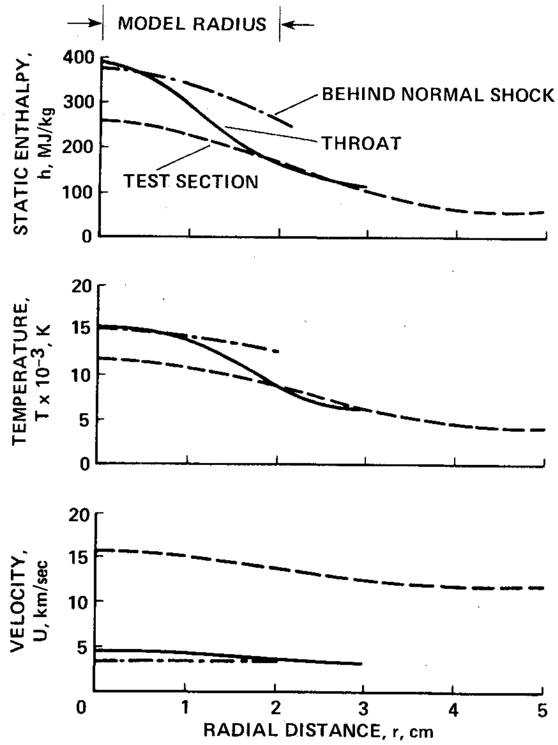

Fig. 7 ARCNOZ solution for the ablation test condition.

tests measure the average values over radial distances of up to 1.0 cm. It is known in the radiative transfer theories that the largest contribution to the radiative heat flux comes from the 45 deg direction. Therefore, for the calculation of convective and radiative heat-transfer rates to the stagnation region in the present experiment, the averages of the flow properties in the range of radius of 0-1.5 cm must be used. Table 1, therefore, lists the average properties in the freestream over this range.

Interpretation of Spectral Data

Shock standoff distance, which controls the radiative heat-transfer rate, and radial velocity gradient, which controls the convective heat-transfer rate, are both related to the curvature of the bow shock wave. For an arbitrarily shaped blunt body, an equivalent hemisphere can be defined that corresponds to the actual curvature of the shock wave. For a flat disk, this relationship is expressed in terms of the average density ratio across the shock ϵ, i.e., the ratio between the freestream density and the average density between the aftershock point and the (inviscid) stagnation point. According to Park,[11] the equivalent nose radius R_n is related to the disk radius R_d by

$$\frac{R_n}{R_d} = \frac{1+\epsilon}{\sqrt{\epsilon}(1-2\epsilon+5.5\epsilon^2)}$$

The disk radius is taken to be 1.9 cm in the present work, accounting for the rounding of the corner (see above subsection on ablation measurements). Shock standoff distance Δ is given by

$$\Delta/R_d = \sqrt{\epsilon}(1+\epsilon)$$

Shock radius is obtained by adding the shock standoff distance to the nose radius. For the conditions of the ablation tests in the present work, these parameters were $\epsilon = 0.210$, $R_n = 6.09$, $\Delta = 1.06$ cm, and $R_s = 7.15$ cm.

As mentioned earlier, the calorimeter model had a surface radius of curvature of 20 cm. The change in shock curvature due to this surface curvature is calculated from the mass conservation relationship. One first derives the expression for the "new" shock standoff distance produced as a result of the surface curvature. The expression contains the new unknown shock radius as a parameter. Separately, the change in radial acceleration is expressed in terms of the new shock radius. One then invokes the mass conservation law, which requires that the fractional change in radial acceleration equals in magnitude the fractional change in shock standoff distance and is opposite in sign. By solving for the new shock radius R_s', one obtains:

$$\frac{R_s'}{R_s} = 1 - \frac{R_d}{\Delta}\frac{R_d}{R_f}\left\{1+\frac{R_s}{\Delta}\left[\sqrt{1-(R_d/R_s)^2}-1\right]\right\}^{-1}$$

where R_f is the radius of curvature of the model surface. For the present case, one has $R_s'/R_s = 0.956$. The equivalent nose radius and shock standoff distance for the calorimeter are $R_n' = 5.82$ cm and $\Delta' = 1.01$ cm, respectively.

The relative radiation spectra emitted by the shock layer flow and received by the spectrometer are calculated for the wavelength range of 390-500 nm for the purpose of comparison with the experimental data of Fig. 4. The calculation is made using the following methods:

1) The radiation is assumed to be optically thin.

2) For the volume integration of the emissions from different parts of the shock layer, the shock layer is divided into nine concentric cylindrical ring elements. The properties are assumed to be constant within each ring and are determined by averaging between the aftershock and the (inviscid) stagnation values. Radiation from each ring is added and weighted with its volume to obtain the total radiation entering the spectrometer.

3) Radiation emanating from the small volume of the freestream in front of the shock layer is accounted for in the same manner. The length of the emitting cylinder is assumed to be 1 cm in this case.

4) The calculation is carried out using the line-by-line radiative transfer code ARCRAP, accounting for the lines and continua of hydrogen.[12]

The results of these calculations are shown in Fig. 8 and are compared with the experimental data. The agreement is generally good. In Fig. 8a, the experimental data are not shown for wavelengths shorter than 408 nm, because experimental data are not accurate there (see above subsection on spectrometric measurement). The small peak in intensity at 485 nm in Fig. 8b is believed to be due to N_2^+ first-negative band radiation. As mentioned earlier (see subsection on the facility), nitrogen is injected into the test section box. The gas is probably entrained by the jet, is heated, and emits the observed radiation. The small discrepancy in the peak intensity of the H_δ line at 410 nm in Fig. 8a is due to the inadequacy of the computational method in this wavelength region in calculating the merging of the highly excited states of hydrogen. The shapes of the H_β and H_γ lines are the most reliable because the theoretical shapes of these lines are accurately known. The good agreement between the measured and calculated line profiles for these two lines is a verification of the validity of the flowfield model used in the present work.

Heat Transfer and Ablation

The flow in the stagnation region over the two geometries of the present experiment (curved disk for the calorimeter and flat disk for the ablation tests) is solved using the code RASLE. The solutions are obtained for the freestream conditions identified as the ablation test case in Table 1. The thermodynamic data[10] for C_2H, C_3H, and C_4H and the radiation absorption by C_3 in the ultraviolet wavelength range[13,14] are accounted for in the calculation. The calculation is carried out for four cases: nonablating tungsten,

Table 2 RASLE solutions for ablation tests (input power = 71 MW)

	Tungsten calorimeter	Graphite and carbon-carbon		Carbon-phenolic	
Property	No blowing	No blowing	Steady-state	No blowing	Steady-state
Radiative heat flux at interface, kW/cm^2	6.76	6.98	7.39	6.98	7.34
Radiative heat flux at wall, kW/cm^2	6.61	6.85	4.94	6.85	5.79
Wall convective heat flux, kW/cm^2	13.9	11.8	0.646	11.8	0.327
Wall temperature, K	2000	4094	4278	4094	4203
Ablation rate $\dot{m}$, g/cm$^2\cdot$s	0	0	0.154	0	0.170
Blowing parameter $B' = \dot{m}/(\rho_\infty V_\infty C_n)$	0	0	8.65	0	18.7
Radiative blockage factor	0.978	0.981	0.668	0.981	0.788
Convective shielding factor	1.0	1.0	0.0547	1.0	0.0277

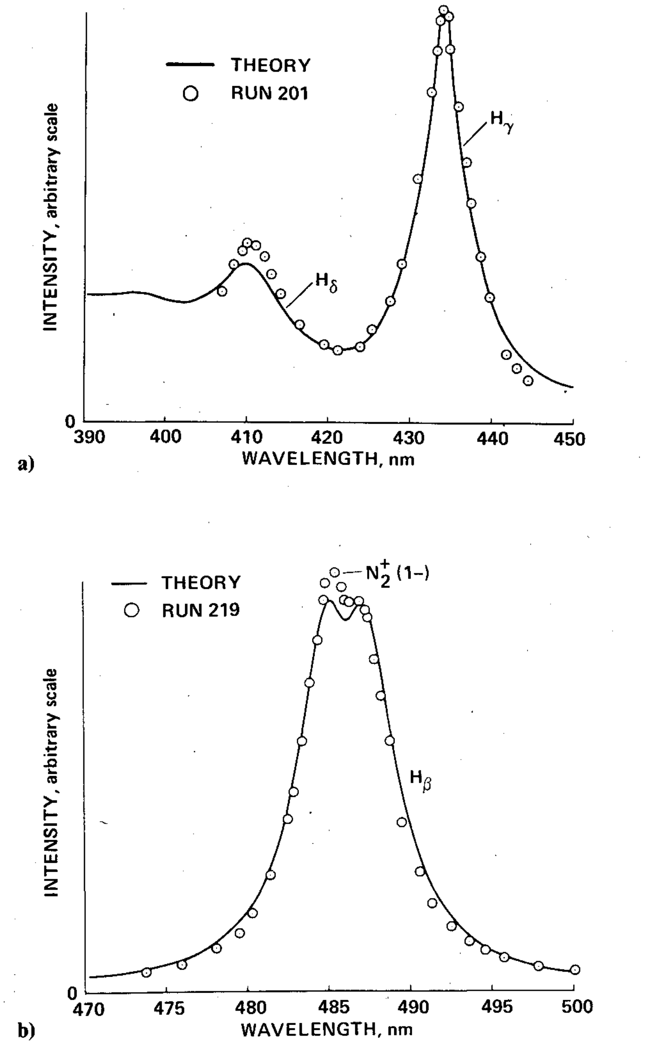

Fig. 8 Comparison between the theoretical and experimental spectra of radiation from shock layer.

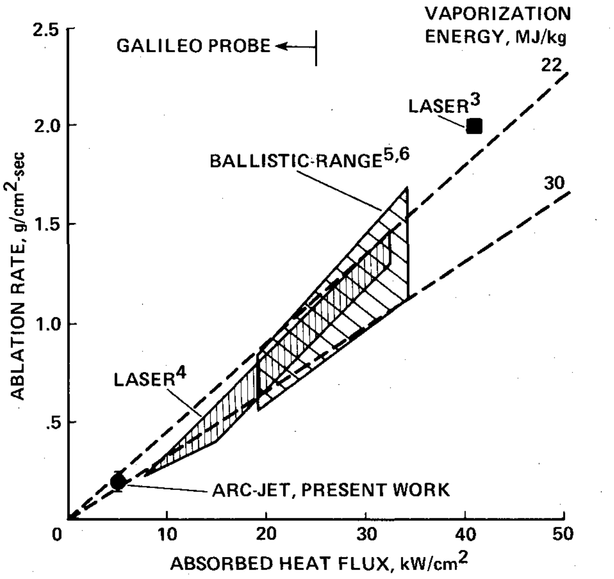

Fig. 9 Comparison among the ablation rates for carbon-phenolic measured by arcjet, laser irradiation, and ballistic range methods.

nonablating carbon (graphite and carbon-carbon) or carbon-phenolic, carbon in steady-state ablation, and carbon-phenolic in steady-state ablation. The shock radii given in the preceding section are given as inputs. For the case of tungsten, the surface temperature and spectral emissivity are the same as in the work of Green and Davy.[9] For carbon and carbon-phenolic, the surface spectral emissivity is assumed to be constant at 0.85. The results of these calculations are summarized in Table 2. The heat-transfer rates for the tungsten case are plotted in Fig. 2 and compared with the measured data.

In Fig. 2, the straight dashed lines are shown for reference only. As the figure shows, the calculated heat-transfer rate values are consistent with the measured values. As mentioned earlier, the experimental total heat-transfer rates include only 78% of the radiative component. When correction is made to account for this fact, agreement between theory and experiment is good.

Under the steady-state ablating conditions, however, the convective heat-transfer rates decrease by an order of magnitude from the nonablating values because of the convective shielding effect of blowing. The blowing parameter $B' = \dot{m}/(\rho U C_h)$, where $\dot{m}$ is the ablation rate and C_h the heat-transfer coefficient, reaches moderate values of 6 and 14. As a result, the convective component of the heat flux is negligible at the wall. Due to absorption by the ablation-product gases in the blowing layer, the radiative heat fluxes reaching the wall are roughly three-quarters of those incident on the interface between the inviscid and the blowing layers. These phenomena are qualitatively the same as those expected to occur during the Jovian entry flight. However, the absolute magnitudes of the heat-transfer and ablation rates are considerably smaller than the peak values encountered in the Jovian flight.

For carbon and carbon-phenolic, ablation behavior is calculated using the CMA code. The properties of the two materials are taken to be the same as those used in the work of Park.[5,6] The radiative blockage factor (the ratio of the radiative heat flux reaching the wall to that at the interface) is assumed to vary as

$$\text{Radiative blockage factor} = \exp(-C\dot{m})$$

This relationship is a special case of Beer's law of radiation absorption and holds rigorously if the optical depth of the blowing layer is proportional to the ablation rate. The constant C in the above equation is chosen so as to be compatible with the RASLE solutions obtained. The convective shielding factor is calculated using the well-known formula.[15] The heat-transfer rates so determined are then given as inputs to the CMA code.

The results of the CMA calculations are presented in Figs. 5 and 6 and are compared with the experimental data. For carbon-phenolic, the steady-state and the CMA solution are nearly the same, corresponding to a heat of ablation of about 30 MJ/kg. For all tested materials, the measured mass loss rates are about 15% higher than the theoretical values. This discrepancy may be attributed to spallation. The carbon-phenolic materials show about 25% higher ablation rates than either graphite or carbon-carbon. This difference in ablation performance between the two groups of materials is well within the common expectations of the materials.

Discussion

The good agreement between theory and experiment in the spectral data (Fig. 8) and heat-transfer rates (Fig. 2) provides confidence in the present method of evaluation of the ablative performance of the tested materials. The small discrepancy between the theoretical and experimental ablation rates is presently attributed to spallation. As mentioned earlier, the ablating surface of the models was fairly smooth after the test. It is not known how spallation occurs without leaving a roughened surface, but such a phenomenon has been known to exist for graphite[16] and hence is not new.

In Fig. 9, the present ablation data for carbon-phenolic are compared with the two other sets of data taken under radiative heating environments, i.e., the laser irradiation[3,4] and ballistic range[5,6] data. The two dashed lines in the figure correspond to the effective heats of vaporization of 22 MJ/kg used in the earlier calculations of the Galileo Probe heat shield and 30 MJ/kg resulting from the present thermodynamic model. The ballistic range data were interpreted using the same thermodynamic model, which leads to a vaporization energy value of 31 MJ/kg in the high-pressure environment of the experiment.[5,6] The laser results[3] obtained at heat fluxes higher than 41 kW/cm^2 are not compared here because the data are subject to an uncertainty as to how much of the laser power reached the wall of the test specimen: at such high heat fluxes, the rate of spallation is so great that the spalled particles partly block the oncoming laser beam. The ballistic range values shown in the figure are obtained by multiplying the theoretical recession rates[5] by the ratio of the overall measured recession to the theoretical recession.[6]

As the figure shows, the three sets of data are consistent and form a continuous trend. At low wall heat fluxes, the measured ablation rates follow the 30 MJ/kg reference line. At high heat fluxes, the measured ablation rates approach the 22 MJ/kg line. The observed agreement at low heating rates lends support to the ablation energy value of 30 MJ/kg and the associated new thermodynamic data for C_2H, C_3H, and C_4H used here.[10] Based on the heat of ablation value of 30 MJ/kg, the spallation rate is about 15% of the total ablation rate at wall heat fluxes of about 20 kW/cm^2 and about 30% at fluxes above 30 kW/cm^2. It was shown earlier that the thickness of the heat shield on the Galileo Probe contains a sufficient margin of safety to allow for spallation of the magnitudes observed here.[4] The present test results reinforce that conclusion.

Conclusions

An ATJS graphite, a carbon-carbon composite, and four types of carbon-phenolic materials are heated in the stagnation region of a blunt body in an arcjet wind tunnel stream of hydrogen/helium mixture. The tested conditions are: total enthalpy $\cong$380 MJ/kg, impact pressure $\cong$ 3 atm, and Mach number $\cong$ 2.1. The wall heating is almost entirely by radiation and its rate is about 6 kW/cm^2. Compared with the theoretical predictions made using the RASLE and CMA codes, the tested materials ablate at a rate about 15% faster. The measured ablation rates agree with those obtained in a laser irradiation facility and in a ballistic range.

References

[1] Howe, J. T., Pitts, W. C., and Lundell, J. H., "Survey of the Supporting Research and Technology for Thermal Protection of the Galileo Probe," AIAA Paper 81-1068, June 1981.

[2] Menees, G. P., "An Evaluation of Computer Codes for Simulating the Galileo Probe Aerothermal Entry Environment," AIAA Paper 81-1069, June 1981.

[3] Lundell, J. H. and Dickey, R. R., "Response of Heat-Shield Materials to Intense Laser Radiation," *Progress in Astronautics and Aeronautics: Outer Planet Entry Heating and Thermal Protection,* Vol. 64, edited by R. Viskanta, AIAA, New York, 1979, pp. 193-209.

[4] Lundell, J. H., "Spallation of the Galileo Probe Heat Shield," AIAA Paper 82-0852, June 1982.

[5] Park, C., "Stagnation-Point Ablation of Carbonaceous Flat Disks: Part 1, Theory," *AIAA Journal,* Vol. 21, Nov. 1983, pp. 1588-1594.

[6] Park, C., "Stagnation-Point Ablation of Carbonaceous Flat Disks: Part 2, Experiment," *AIAA Journal,* Vol. 21, Dec. 1983, pp. 1748-1754.

[7] Winovich, W. and Carlson, W. C. A., "The Giant Planet Facility," Paper presented at 25th Instrument Society of America Symposium, Los Angeles, April 1979.

[8] Davy, W. C., Menees, G. P., Lundell, J. H., and Dickey, R. R., "Hydrogen-Helium Ablation of Carbonaceous Materials: Numerical Simulation and Experiment," *Progress in Astronautics and Aeronautics: Outer Planet Entry Heating and Thermal Protection,* Vol. 64, edited by R. Viskanta, AIAA, New York, 1979, pp. 228-244.

[9] Green, M. J. and Davy, W. C., "Numerical Simulation of Experiments in the Giant Planet Facility," *Progress in Astronautics and Aeronautics: Entry Heating and Thermal Protection,* Vol. 69, edited by W. B. Olstad, AIAA, New York, 1980, pp. 172-197.

[10] Moss, J. N. and Simmonds, A. L., "Galileo Probe Forebody Flow Field Predictions During Jupiter Entry," AIAA Paper 82-0874, June 1982.

[11] Park, C., "Calculation of Radiation from Argon Shock Layers," *Journal of Quantitative Spectroscopy and Radiative Transfer,* Vol. 28, No. 1, July 1982, pp. 29-40.

[12] Arnold, J. O., Cooper, D. M., Park, C., and Prakash, S. G. "Line-by-Line Transport Calculations for Jupiter Entry Probes," *Progress in Astronautics and Aeronautics: Entry Heating and Thermal Protection,* Vol. 69, edited by W. B., Olstad, AIAA, New York, 1980, pp. 52-82.

[13] Prakash, S. G. and Park, C., "Shock Tube Spectroscopy of $C_3 + C_2H$ Mixture in the 140-700 nm Range," AIAA Paper 79-0094, Jan. 1979.

[14] Shinn, J.L., "Optical Absorption of Carbon and Hydrocarbon Species from Shock Heated Acetylene and Methane in the 135-200 nm Wavelength Range," AIAA Paper 81-1189, June 1981.

[15] Dorrance, W. H., *Viscous Hypersonic Flow,* McGraw-Hill Book Co. New York, 1962, pp. 112-114.

[16] Lundell, J. H. and Dickey, R. R., "Ablation of ATJ Graphite at High Temperatures," *AIAA Journal,* Vol. 11, Feb. 1973, pp. 216-222.